Chemical Engineering Journal 446 (2022) 136912

Contents lists available at ScienceDirect

Chemical Engineering Journal

journal homepage: www.elsevier.com/locate/cej

Eu(II)-MOF as NIR probe for highly efficient instantaneous anodic electroluminescence realized environmental pollutant trace monitoring

Lu Zhao, Xianzhen Song, Huan Wang, Xueying Wang, Dan Wu *, Qin Wei, Huangxian Ju

Collaborative Innovation Centre for Green Chemical Manufacturing and Accurate Detection, School of Chemistry and Chemical Engineering, University of Jinan, Jinan 250022, Shandong, China

ARTICLE INFO

Keywords:
Eu(II)-MOF
NIR probe
ECL sensor
Environmental trace monitoring

ABSTRACT

One of the effective ways to prevent environmental pollutants from entering the human body and causing cancer is to detect them efficiently and sensitively in the external environment, even trace detection. Herein, we developed a rare Eu(II)-MOF (Eu(II)-Phen) as near infrared (NIR) probe to construct high instantaneous anodic electrochemiluminescence (ECL) sensor for trace detection of environmental pollutants. Eu(II)-Phen was synthesized by the reductant of glycine and the protectant of oleylamine, which avoided using a large amount of inert gas to prevent Eu^{2+} from oxidizing into Eu^{3+}. The Eu(II)-Phen possessed high-efficiency ECL with the aid of tripropylamine (TPA) coreactant, which was certified by DFT, electrochemical and ECL characterization. Then, the double enhancement mechanism prompted the ECL efficiency to enhance: i) the high energy transfer efficiency brought from the antenna effect of ligand to Eu^{2+}, ii) the faster and more generation of coreactant radical ($TPA^{\bullet}$) catalyzed by Fe_3O_4-Ag NRs. Moreover, under NIR emission, the constructed ECL sensor with Eu(II)-Phen can work stably in the harsh environment such as heavy pollution. Given its high instantaneous luminous efficiency, NIR emission, self-enhancement and designable merits, the constructed ECL sensor represents a promising practical platform for trace environmental monitoring to prevent pollutants from attacking the human body.

1. Introduction

In the near infrared (NIR) luminescence materials, luminescent lanthanide complexes (LLCs), such as $Tb(pzda)_3(NO_3)_3{\cdot}nH_2O$ [1], Ln $(DBM)_3$bath [2], Ir^{III}-Eu^{III}DOTA [3], have possessed immense attention by right of their inherent luminescence superiorities (high luminous efficiency, long lifetime and innate narrow emission peak) [4-6]. Among them, lanthanide metal–organic frameworks (Ln-MOFs), with merits of the good electroconductivity and ample active sites of MOFs [7-9], stand out from the LLCs and are better suited to ECL luminescence. In our previous works, we constructed the NIR ECL sensors by preparing Eu (III)-MOFs as luminophors [10-12]. The high luminescence efficiency makes the NIR ECL sensors have outstanding sensitivity and accuracy, which can meet the environmental trace detection. In addition to Eu^{3+}, due to spin-allowed nature and the stabilization of the 5*d* orbitals, Eu^{2+} has the characteristic of 5*d*–4*f* transition, therefore Eu^{2+} can be applied into fluorescent lamps, plasma display panels, luminophors of fluorescence and ECL sensors [13,14]. However, because the Eu^{2+} is easily oxidized into Eu^{3+} ($\varphi_{Eu^{3+}/Eu^{2+}} = -0.38$ V), the preparation conditions of Eu(II)-MOFs are harsh, and the utilization of Eu^{2+} is mostly in the form of ion doping (such as $Ba_3Ln(PO_4)_3$:Ce^{3+})[13-16]. Till now, only few pure Eu(II)-MOFs were reported. For example, Liu et al. reported a series of EuX_2-Nn (X = Br, I, n = 4, 8) with high efficiency and luminance. The optimal performance of EuI_2-N_8 were 25470 cd m^{-2} maximum luminance, 62.4 cd A^{-1} current efficiency and 17.7% external quantum efficiency, respectively [16]. Albrecht-Schönzart et al. reported [Eu (2.2.2B)Cl][BPh_4]·2CH_3OH and [Eu(2.2.2B)(CH_3OH)][BPh_4] 2·CH_3OH cryptate MOFs with 2.2.2B cryptand as ligand [17]. Therefore, it is promising for exploiting an easily prepared and Eu(II)-MOFs to realize efficient luminescence.

The particular 5*d*–4*f* transition of Eu^{2+} endows it with some unique virtues compared to Ln^{3+} and other luminophors, such as the weak excited state quenching, the electronic stability, the higher maximum luminance and electronic stability, which due to the spin-allowed character and the open-shell electron transition form [16,18,19]. In addition, the 5*d* level is near or below $6P_{7/2}$, decreasing the multiphoton relaxation and enhancing instantaneous luminous efficiency [20]. Meanwhile, the Eu^{2+} owns a $4f^7$ system, corresponding to a half-filled 4*f*

* Corresponding author.
E-mail address: wudan791108@163.com (D. Wu).

https://doi.org/10.1016/j.cej.2022.136912
Received 27 February 2022; Received in revised form 14 April 2022; Accepted 7 May 2022
Available online 10 May 2022

subshell, adding to its electronic stability [17]. Low valence metal ions may lose electrons to form radicals at a certain positive potential, so as to realize anodic luminescence. Hitherto, the vast majority of Eu-MOFs used in ECL field are restricted to the applications of cathode. Therefore, the Eu(II)-MOFs with high anodic instantaneous ECL efficiency undoubtedly broaden the application range of Eu-MOFs and inject new candidates for the construction of efficient ECL sensors to be more suitable for rapid response or detection.

Thanks to the electron loss process, Eu(II)-MOFs may achieve infrequent anodic ECL of Eu-MOFs, which needs the help of coreactants like H_2O_2 or tripropylamine to improve the efficiency and sensitivity of the luminophore-coreactant ECL system [21]. The increase of yield and the acceleration of production speed for coreactant radicals can improve the efficiency and sensitivity of the luminophore-coreactant ECL system. A high-efficiency approach for increasing yield and accelerating production speed of coreactant radicals is that using the catalysts with high performance [22,23]. Fe-based catalysts harvest extensive attention powered by their good and unique natures [24]. Among them, Fe_3O_4 has possessed massive attention in catalysis, sensing, magnetic separation, drug/gene delivery with merits of its high relaxivity, insoluble property and low toxicity [25,26]. In addition, Ag NPs can connect with the amino group attached to antigen, antibody and proteins, thus Ag NPs are widely applied in sensing, clinical imaging, etc.. Moreover, Ag NPs as a precious metal also have good catalytic properties [27]. To sum up, the nanocomposites made up of Fe_3O_4 and Ag NPs can improve catalytic efficiency and ECL performance to better meet the needs of rapid and sensitive environmental detection.

With the development of human society, the impact of new environmental pollutants on humans and animals is becoming more and more serious. Among them, especially the environmental estrogen, will harm the human endocrine and reproductive system, affect the hormonal balance of organism, which appear phenomena of bisexual individuals, a substantial reduction in male individual number, feminization of the male body and shortness of male genitalia [28-30]. Trenbolone is one of the new environmental estrogens, which is known as the perfect steroid to be widely used in sports, fitness and graziery industry to promote muscle growth to advance the meat production rate. Negative effects on the environment are brought from the massive use and discharge of trenbolone, thus triggering a demand for trace detection of trenbolone in water resources [31-33].

Based on the above thoughts, a pure Eu(II)-MOFs, with high instantaneous luminous efficiency, was synthesized by 1,10-phenanthroline as ligand and depended on reductant glycine and protectant oleylamine, realizing anodic ECL of Eu(II)-MOFs for the first time. The Eu(II)-MOFs with NIR characteristic endowed the constructed ECL sensor loose operating conditions, so that the sensor can detect pollutants in harsh environment, such as high temperature, high pressure, heavy pollution, etc. [10-12]. The constructed ECL sensor can satisfy the trace detection of trenbolone commendably with a low limit of detection (LOD, 4.42 fg/mL) and a broad detection range from 10 fg/mL to 100 ng/mL, and even can extend to highly efficient and sensitive detection of other environmental pollutants.

2. Experimental section

2.1. Preparation of Ag NRs.

Ag NRs was synthesized according to the literature with some modifications [34]. 0.01 mM $FeCl_3$ solution was prepared with glycol, and then 20 mL $FeCl_3$ solution was added 1.665 g PVP to form the solution a. 20 mL 0.1 M $AgNO_3$ solution was prepared with glycol and named the solution b. Next the solution a was added into solution b drop by drop under continuous stirring, the final solution was reacted in Teflon-lined stainless steel autoclave at 160 °C for 3 h. The bright silver powders were centrifuged by ethanol and dried overnight at 60 °C.

2.2. Preparation of Fe_3O_4-Ag NRs.

Fe_3O_4-Ag NRs was synthesized according to the literature with some modifications [34]. 0.023 g of $FeCl_3{\cdot}6H_2O$ and 0.012 g of $FeSO_4{\cdot}7H_2O$ were dissolved in 14 mL of glycol, and then the mixed solution was heated at 50 °C under continuous stirring. 0.1 g as-prepared Ag NRs was dispersed in 10 mL of glycol and dropwise added into the aforesaid solution. The final solution was heated at 65 °C under continuous stirring for 20 min. Next, the final solution was mixed with a solution of NaOH prepared by glycol (0.1 g NaOH dissolved in 5 mL glycol) and stirred for 20 min at same temperature. In the end, the solution was transferred into a Teflon-lined stainless steel autoclave and reacted for 4 h at 200 °C to form black Fe_3O_4-Ag NRs after centrifugal washing several times via ethanol.

2.3. Preparation of Eu(II)-Phen.

The preparation diagram was displayed in Scheme 1A. 1 mmol $EuCl_3{\cdot}6H_2O$ and 1 mmol 1,10-Phenanthroline were dissolved in the mixed solution (ethanol: H_2O = 1:1). The 0.3 M NaOH solution was dropped into the mixed solution to pH = 7. Next, 0.5 mmol glycine and 1 mL oleylamine was added into the mixed solution. Finally, the mixed solution was transferred into a round bottom flask and reacted for 2 h at 70 °C and then heated to 130 °C under continuous stirring for 2 h. The white product was obtained after centrifugation and washing several times via water.

2.4. Fabrication of the ECL sensor.

The establishment process of electrode was shown in Scheme 1B. First of all, the bare glassy carbon electrode (GCE) was smoothed with polishing powders. Secondly, 8 μL Fe_3O_4-Ag solution as was dropped on the electrode to connect the TB antibody (Ab) and accelerate the generation of coreactant radical. Next, 4 μL of antibody solution (1 μg/mL), 2 μL of BSA, 6 μL of the mixture of different concentrations TB standard substances and antigen@Eu(II)-Phen (the concentration of antigen was 1 μg/mL) was dropped on electrode successively. After each drip coating, the electrode should be dried at 4 °C, and then washed with water to remove the unbonded parts. Finally, the successfully constructed ECL sensor was placed at 4 °C.

3. Results and discussion.

3.1. Characterization of Eu(II)-Phen.

The XPS survey scan spectrum of Eu(II)-Phen was shown in Fig. S1. In XPS spectrum of Eu 3d (Fig. 1A), two strong binding energy values at 1123.2 and 1152.6 eV are attributable to Eu $3d_{5/2}$ and Eu $3d_{3/2}$ of Eu^{2+}, which accompanied by weak peaks of Eu^{3+} at 1133.5 and 1163.3 eV [11,35]. The weak peaks represented the less content of Eu^{3+}, which was assumed as impurities or raw materials that have not been reduced, confirming the principal status of Eu^{2+} in Eu(II)-Phen. The FT-IR spectra showed the situations of functional groups in 1,10-Phenanthroline and it coordinated with Eu^{2+}. In Fig. 1B, the characteristic peaks of phenanthrene ring (the C = C and C = N stretching vibration of phenanthrene ring) in ligand at 1581 and 1551 cm^{-1} were red-shifted to a wide band at 1515 cm^{-1}, which showed that the N atoms in the phenanthrene ring coordinate with the central Eu^{2+}, resulting in the stretching vibration decreases and the increase of the electron-donate capability of the complex [36]. Meanwhile, this is accompanied by the red-shift of $\delta_{C\text{-}H}$ from 738 cm^{-1} to 725 cm^{-1}. Specially, the new absorption peak at 515 cm^{-1} was attributable to the stretching vibration of Eu-N [37]. In addition, the broad band corresponded to the $V_{O\text{-}H}$ at 3420 cm^{-1} [38]. These results all proved the successful coordination between Eu^{2+} and 1,10-Phenanthroline. In UV–vis spectra (Fig. 1C), the free 1,10-Phenanthroline ligand showed characteristic absorption bands centered at 227

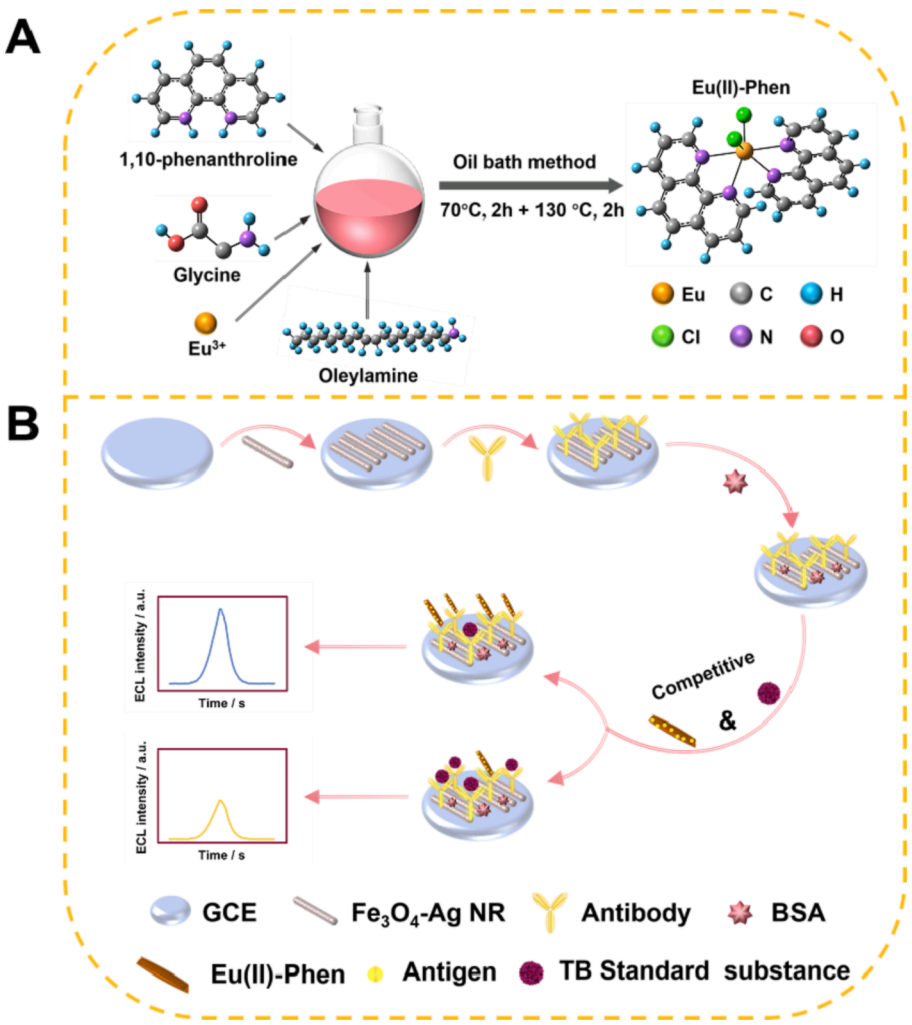

Scheme 1. (A) The synthesis route of Eu(II)-Phen. (B) The ECL sensor fabrication process and competitive mechanism.

and 264 nm. Eu(II)-Phen obtained three narrow absorption bands centered at 204, 268 and 276 nm. Among them, the wide peak of ligand at 264 nm was red-shifted and split to two narrow peaks of Eu(II)-Phen at 268 and 276 nm, which resulted from the coordination of ligands with Eu(II) centers, the ligand-to-metal Eu(II) center charge transfer (LMCT) process and the $4f^7$-$4f^6 5d^1$ transitions of Eu^{2+} [39,40]. The synthesis and optical properties of Eu(II)-MOF were also certified by the Fluorescence excitation emission spectrum (Fig. 1D). Crystalline powder of Eu(II)-Phen shows bright orange emissions with wavelength of 360 nm and 527 nm, respectively. These emissions correspond to the allowed electric-dipole transition $4f^6 5d^1 \rightarrow 4f^7\,{}^8S_{7/2}$ and $4f^6 5d^1 \rightarrow 4f^7 5d^1$ of Eu^{2+}. The excitation bands of Eu(II)-Phen are characteristic Eu^{2+} peak with wavelength of 238 nm and 276 nm, which belong to $4f^7\,{}^8S_{7/2} \rightarrow 4f^6 5d^1$ [13,40,41]. The UV–vis-NIR absorption spectrum of Eu(II)-Phen exhibited a clean NIR-II signal at 1518 nm, while no peaks were observed in NIR region of ligand spectrum, which confirmed the characteristic NIR-II luminescence of Eu(II)-Phen (Fig. 1E-F). In addition, the morphology and size of the Eu(II)-Phen were investigated by SEM imaging (Fig. 1G). It can be seen that the fusiform Eu(II)-Phen nanorods gathered densely to form a bigger fusiform body with a quite uniform size of 100 nm wide and 700 nm long. The width of each monomer fusiform Eu(II)-Phen nanorods is about 25 nm. From the Energy Dispersive Spectrometer (EDS) spectra and mapping result (Fig. 1H-I), the elements of Eu, C, N, Cl contained in Eu(II)-Phen were observed to be present and evenly distributed.

3.2. Characterization of the catalyst.

The Fe_3O_4 nanoparticles grown on the Ag nanorods (Ag NRs) was used for the catalyst to accelerate the generation of $TPA^{\bullet}$. For the verification for successful synthesis of Fe_3O_4-Ag NRs, the X-ray diffraction patterns were used to find out the details of their structural composition and crystal phase information at first. As can be seen from Fig. 2A, four high and sharp peaks at 38.1°, 44.3°, 64.4° and 77.5° were corresponded to crystallographic planes of (111), (200), (220) and (311) respectively, which belonged to Fe_3O_4 (JCPDs no. 85–1436). Meanwhile, five unconspicuous peaks at 30.1°, 35.4°, 43.1°, 57.0° and 62.5° were corresponded to crystallographic planes of (220), (311), (400), (511) and (440) respectively, which belonged to Ag (JCPDs no. 04–0783). The UV–vis absorption spectra confirmed the composite of Fe_3O_4 and Ag NRs (Fig. 2B). The typical absorption peak was detected at 420 nm, symbolizing the surface plasmon resonance of Ag NRs [42]. While loading Fe_3O_4 nanoparticles on Ag NRs, the UV–vis absorption peak was redshifted to about 531 nm, illustrating that the load of Fe_3O_4 nanoparticles increased surface charge and changed basic process of electron-hole pair formation during irradiation [43]. The homogeneous morphology of as-prepared Ag was shown in Fig. 2C, which presented nanorods morphology with unified length of 1.2 μm and width of 125 nm approximately. Next, the sesame stick shape was presented for Ag NRs enfolded small Fe_3O_4 nanoparticles with a diameter of a several nanometers (Fig. 2D). According to energy-dispersive X-ray spectroscopy (EDS) and mapping results (Fig. S3-4), the elements of Ag, Fe and O

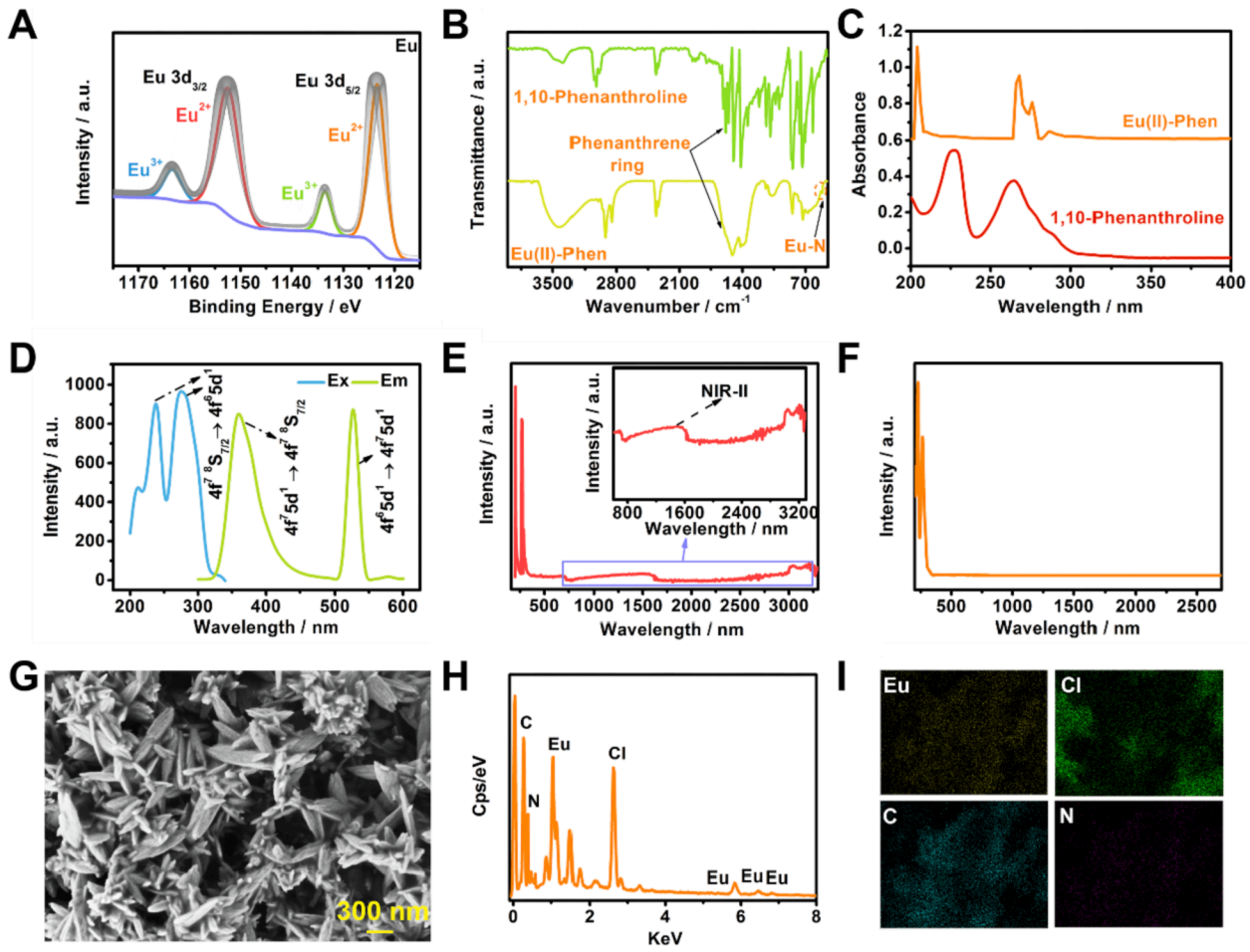

Fig. 1. (A) XPS spectrum in the Eu 3d region for Eu(II)-Phen. (B) FT-IR and (C) UV–vis spectra of Eu(II)-Phen and ligand 1,10-Phenanthroline. (D) Fluorescence excitation emission and (E) UV–vis-NIR spectra of Eu(II)-Phen. (F) UV–vis-NIR spectrum of 1,10-Phenanthroline. (G) SEM image and (H) EDS spectrum of Eu(II)-Phen. (I) EDS elemental mapping images of Eu, C, Cl and N for Eu(II)-Phen.

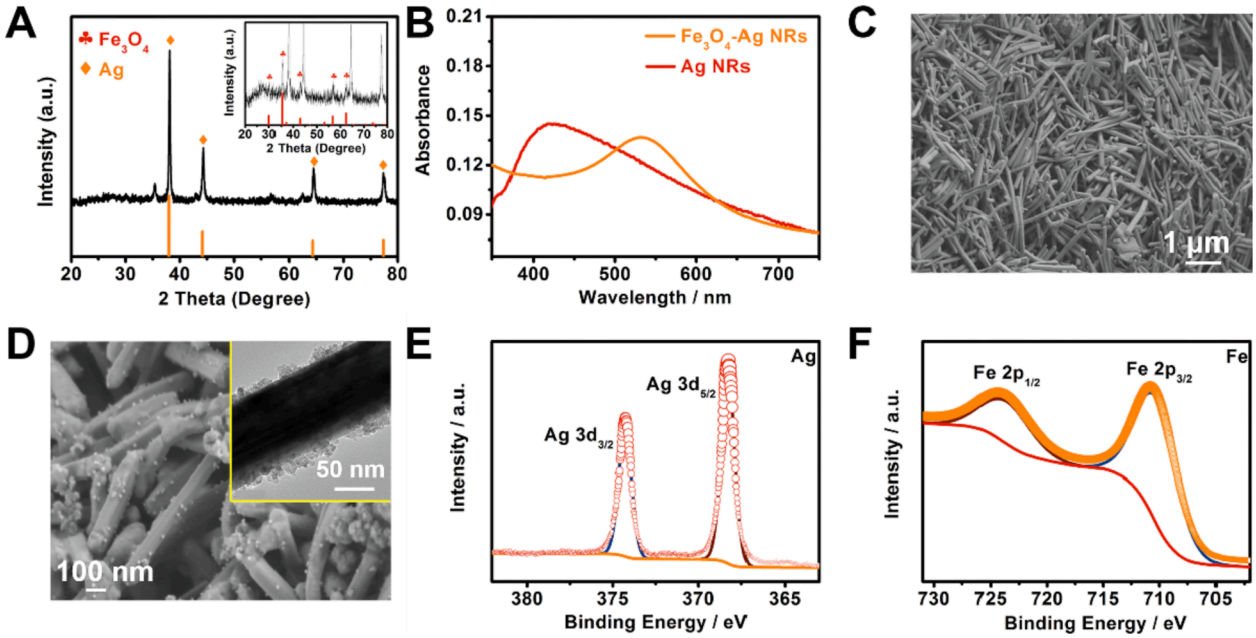

Fig. 2. (A) XRD pattern of as-synthesized Fe_3O_4-Ag NRs and simulated Fe_3O_4 and Ag. (B) UV–vis spectra of Fe_3O_4-Ag NRs and Ag NRs. (C) SEM image of Ag NRs. (D) SEM image of Fe_3O_4-Ag NRs, and the inset figure showed the TEM image of Fe_3O_4-Ag NRs. XPS spectrum in the (E) Ag 3d and (F) Fe 2p regions for of Fe_3O_4-Ag NRs.

in Fe_3O_4-Ag NRs were evenly distributed. With the existences of Fe, O, Ag and C elements, obvious peaks were observed from the XPS survey scan spectrum in Fig. S5A. The high resolution XPS spectrum of Ag 3d for the Fe_3O_4-Ag NRs showed two contributions, Ag $3d_{5/2}$ and Ag $3d_{3/2}$, locating at respectively 368.3 and 374.3 eV (Fig. 2E), which can be assigned to the metallic Ag [34,44]. The binding energy values at 710.8 and 724.4 eV with a spin–orbit splitting of 13.6 eV between Fe $2p_{3/2}$ and Fe $2p_{1/2}$, which matched with the standard reference XPS spectrum of Fe_3O_4 (Fig. 2F) [27,45]. Moreover, in Fig. S5B, the single and high peak of O was observed at 530.2 eV, attributing to the oxygen atoms in Fe_3O_4 [34]. These results were striking evidences for the successful synthesis of Fe_3O_4-Ag NRs.

3.3. *Proof of enhancement of electro-active surface area and electron transfer of Fe_3O_4-Ag NRs.*

To immobilize trenbolone antibody (TB Ab) on electrode surface, Ag NRs were covered on electrode to connect with Ab via Ag-S bonding.

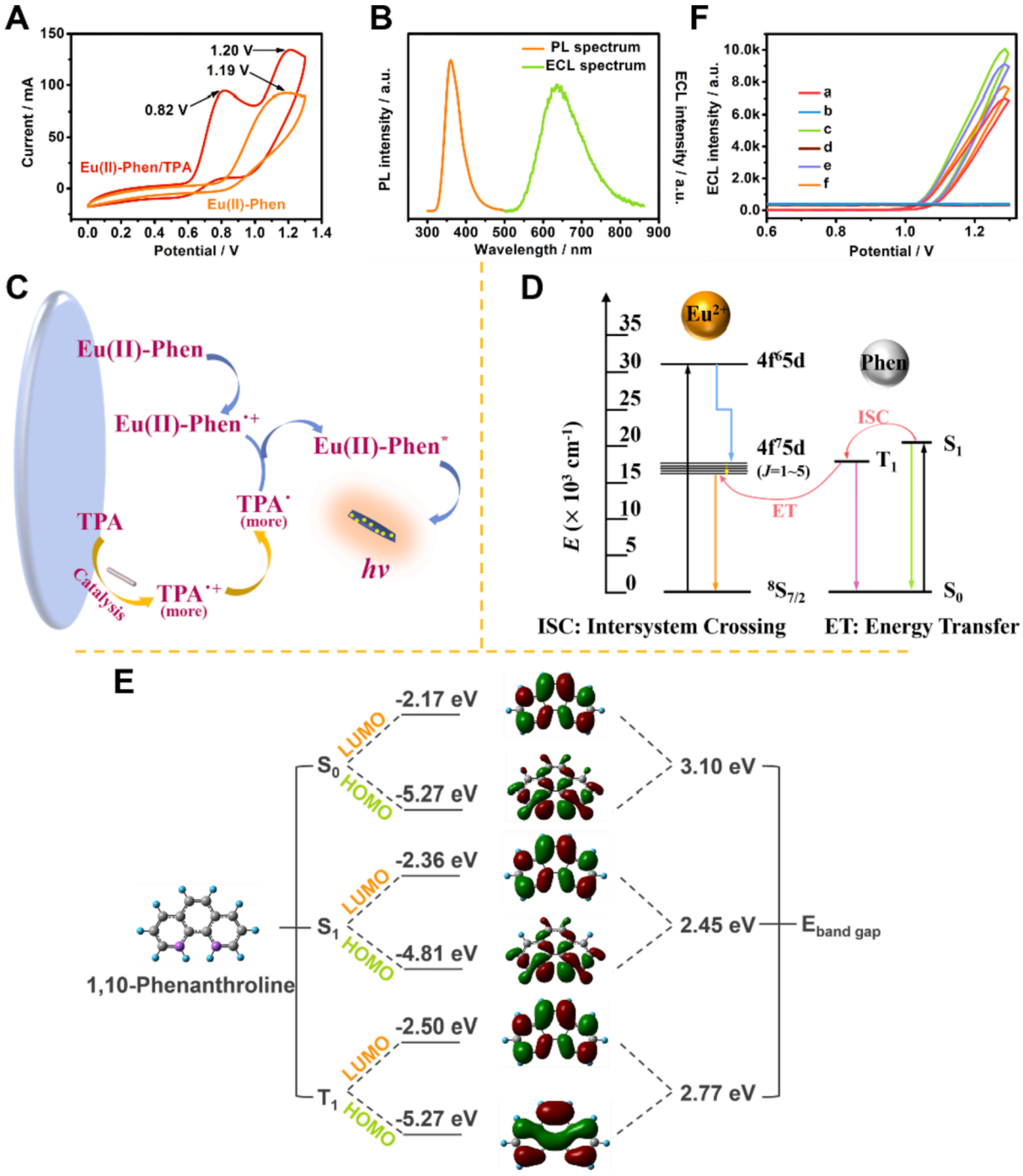

Fig. 3. (A) The CV curves of Eu(II)-Phen with and without TPA. (B) Fluorescence emission (Em) and ECL spectra of Eu(II)-Phen. (C) The supposed ECL schematic diagram of the constructed sensor in TPA. (D) Simple model for energy-transfer processes of ligand to Eu^{2+} and the *f-d* transition emission mechanism of Eu^{2+} in Eu (II)-Phen. (E) The frontier molecular orbitals with their HOMO, LUMO energy levels and band gap energies of S_0, S_1, T_1 in 1,10-Phenanthroline. (F) ECL-potential curves of different modified electrodes: (a) bare Eu(II)-Phen in PBS contained TPA, (b) bare Eu(II)-Phen in PBS, (c) Eu(II)-Phen/Fe_3O_4-Ag NRs in PBS contained TPA, (d) Eu(II)-Phen/Fe_3O_4-Ag NRs in PBS, (e) Eu(II)-Phen/Ag NRs in PBS contained TPA and (f) Eu(II)-Phen/Fe_3O_4 NPs in PBS contained TPA.

Moreover, the Ag NRs can also be used as coreactant accelerator based on their electrochemical property to catalyze the generation of coreactant radicals. However, the traditional fabrication technique may cause the agglomeration of Ag NRs on the surface of the electrode, which may affect the electroconductibility and catalytic activity. The Fe_3O_4 NPs embellished on Ag NRs can make the composite better for catalyzing the generation of coreactant radicals by the good electrocatalytic capacity of Fe_3O_4 and the increscent electrochemically active specific surface area (ECSA) of composite, and ameliorating the agglomeration of Ag NRs. The cyclic voltammetry (CV) tests were used to prove the ECSA and electron transfer of Fe_3O_4-Ag NRs. In Fig. S6, compared with Ag NRs, the current responses of Fe_3O_4-Ag NRs were higher, which demonstrated the faster electron transfer and better electroconductibility of Fe_3O_4-Ag NRs [10,11].

In addition, the values of ECSA were calculated through the slopes of linear relation for reduction peak values vs scan rates and Randles-Sovcik equation [10,11]:

$$I = 2.69 \times 10^5 A D^{1/2} n^{3/2} v^{1/2} c,$$

in which *I, A, D, n, v and c* mean the peak reduction current of $K_3[Fe(CN)_6]$, the ECSA to be calculated, the diffusion coefficient of $[Fe(CN)_6]^{4-/3-}$ at room temperature, the number of electron transfer, the scanning rate during this test respectively and the concentration of $K_3[Fe(CN)_6]$ solution, respectively. The calculated ECSA of Ag NRs and Fe_3O_4-Ag NRs were 2.5 mm^2 and 3.7 mm^2. The increased ECSA and electroconductibility of Fe_3O_4-Ag NRs provided the possibility to catalyze the formation of more coreactant radicals.

3.4. ECL mechanism of Eu(II)-Phen.

The ECL mechanism of Eu(II)-Phen was researched by CV, fluorescence emission spectrum and ECL spectrum. First of all, we tested CV of Eu(II)-Phen in MeCN containing 0.1 M tetra-n-butylammonium perchlorate (orange curve) and in PBS contained 10 mM TPA (red curve). From Fig. 3A, the oxidation peak of Eu(II)-Phen at 1.19 V was observed in the region of 0–1.3 V (orange curve), the similar oxidation peak of Eu(II)-Phen existed in red curve with the oxidation peak of TPA → $TPA^{\bullet+}$ at about 0.82 V, and no reduction peak was observed in red curve, which implied that the holes only injected into the highest occupied molecular orbital (HOMO) of Eu(II)-Phen to form Eu(II)-$Phen^{\bullet+}$ [12]. Meanwhile, the similar-trending fluorescence emission spectrum and ECL spectrum with maxima of 360 and 662 nm respectively demonstrated that the excited state of Eu(II)-Phen (Eu(II)-Phen*) for ECL emission generated by the band gap transition (Fig. 3B) [46]. Based on these, we speculated that the creation of the exited state of Eu(II)-Phen (Eu(II)-Phen*) and its subsequent luminesce was achieved with the aid of TPA. The relevant ECL mechanism was shown in the Fig. 3C and formulas (1) ~ (6) [21,47]:

$$\text{Eu(II)-Phen} - e^- \rightarrow \text{Eu(II)-Phen}^{\bullet+} \quad (1)$$

$$\text{TPA} - e^- \rightarrow \text{TPA}^{\bullet+} \text{ (more)} \quad (2)$$

$$\text{TPA}^{\bullet+} - H^+ \rightarrow \text{TPA}^{\bullet} \text{ (more)} \quad (3)$$

$$\text{TPA}^{\bullet} - e^- \rightarrow P_1 \quad (4)$$

$$\text{Eu(II)-Phen}^{\bullet+} + \text{TPA}^{\bullet} \rightarrow \text{Eu(II)-Phen*} + P_1 \quad (5)$$

$$\text{Eu(II)-Phen*} \rightarrow \text{Eu(II)-Phen} + h\nu \quad (6)$$

The self-enhancement ECL mechanism of the constructed sensor was realized by the antenna effect of ligand to Eu^{2+}, the LMCT process was verified by UV–vis and fluorescence excitation emission spectra (Fig. 1C and D). The Gaussian09 program was utilized to verify the antenna effect theoretically. Specifically, the density functional theory (DFT) calculations were proceeded by PBEPBE method and 6–31 G* basis set [48] to calculate the HOMO and LUMO energy levels and energies of ground state (S_0), singlet state (S_1) and triplet first excited state (T_1) of 1,10-Phenanthroline. As can be seen in Fig. 3D, the ligand 1,10-Phenanthroline was excited to its S_1 with an excitation energy of 20035.62 cm^{-1}, next the electrons were transferred to triplet state (T_0) and arrived T_1 with a phosphorescent emission energy of 17996.65 cm^{-1} through intersystem crossing (ISC), and then the energy was transferred from T_1 to appropriate $4f^7 5d$ ($J = 5$) vibrational level of Eu^{2+} by nonradiative energy transmission. Powered by the sensitization of 1,10-Phenanthroline, Eu^{2+} released strong luminescence and returned to its ground state of $^8S_{7/2}$. The energy of T_1 of 1,10-Phenanthroline was larger than the excited state energy of Eu^{2+} but the energy difference existed in a certain range, and the higher LUMO energy level of 1,10-Phenanthroline than Eu^{2+} demonstrated jointly a possible electron transfer from ligand 1,10-Phenanthroline to Eu^{2+}. The HOMO and LUMO energy levels and band gap energies of S_0, S_1 and T_1 in 1,10-Phenanthroline were shown in Fig. 3E.

Another self-enhancement ECL mechanism is to promote the more and faster generation of TPA radicals ($TPA^{\bullet}$) powered by the catalysis of Fe_3O_4-Ag NRs. From the ECL-potential curves with different modified electrodes (Fig. 3F), the coreactant function of TPA was verified in the same modified electrodes with and without TPA (curve a-b). Further, the ECL signals were improved under the effect of Fe_3O_4-Ag NRs (curve c-d). Meanwhile, the amplification effect of Fe_3O_4-Ag NRs on the ECL signals is significantly better than that of single Ag NRs (9104 a.u.) or Fe_3O_4 NPs (7538 a.u.) (curves e and f). Furthermore, low and undifferentiated ECL signals of curves b and d (ECL systems without TPA) proved the single catalysis of Fe_3O_4-Ag NRs on TPA rather than Eu(II)-Phen.

3.5. ECL efficiency of Eu(II)-Phen.

To measure the ECL efficiency (Φ_{ECL}) of Eu(II)-Phen, we conducted ECL test and CV test for the constructed ECL sensor and calculated Φ_{ECL} by the equation [12]:

$$\Phi_{ECL} = \Phi^{\circ}_{ECL}\left(IQ^{\circ}_f / Q_f I^{\circ}\right)$$

. Specifically, the Φ°_{ECL} represents the ECL efficiency in the reference system. The reference system is 1 mM $[Ru(bpy)_3]^{2+}$ in 0.1 M (TBA)BF_4/acetonitrile solution, and the Φ°_{ECL} is 5.0%. I and I° are the ECL responses in the Eu(II)-Phen/TPA and reference systems respectively, Q_f and Q°_f are the corresponding faradaic charge passed for them. The calculated Φ_{ECL} of Eu(II)-Phen is about 12.6%, demonstrating Eu(II)-Phen possesses high instantaneous ECL efficiency in TPA, which was much higher than that of the other luminophors of $[Ru(bpy)_3]^{2+}$ and its derivants, and the comparison results were exhibited in Table S1. These made the constructed ECL sensor with Eu(II)-Phen can be applied to rapid and sensitive environmental detection.

3.6. Application of ECL sensor for TB.

We carried out optimal experiments for operating conditions of the constructed ECL (Fig. S7) and the quantitative detection for TB under the optimized environment. The successful construction of the ECL sensor was proved via CV and EIS (Fig. S8), the construction process and competitive sensing mechanism of the ECL sensor was showed in Scheme 1B. The competition scene has formed because of the competitive specific binding of TB antigen and standard substance to TB antibody, therefore the ECL signals were directly related to the concentration of TB standard substance, which resulted in a degressive signal trend as the TB concentration increased. This phenomenon was intuitively reflected via three-dimensional working curves and their corresponding linear relation. As shown in the Fig. 4A-B, the ECL signals decreased linearly with the linear relation of $I = 11919.0 \lg c - 906.0$ ($R^2 = 0.992$) in the same time period. The resulting detection limit is 4.42 fg/mL, which was lower than the reported detection methods for TB (Table S2).

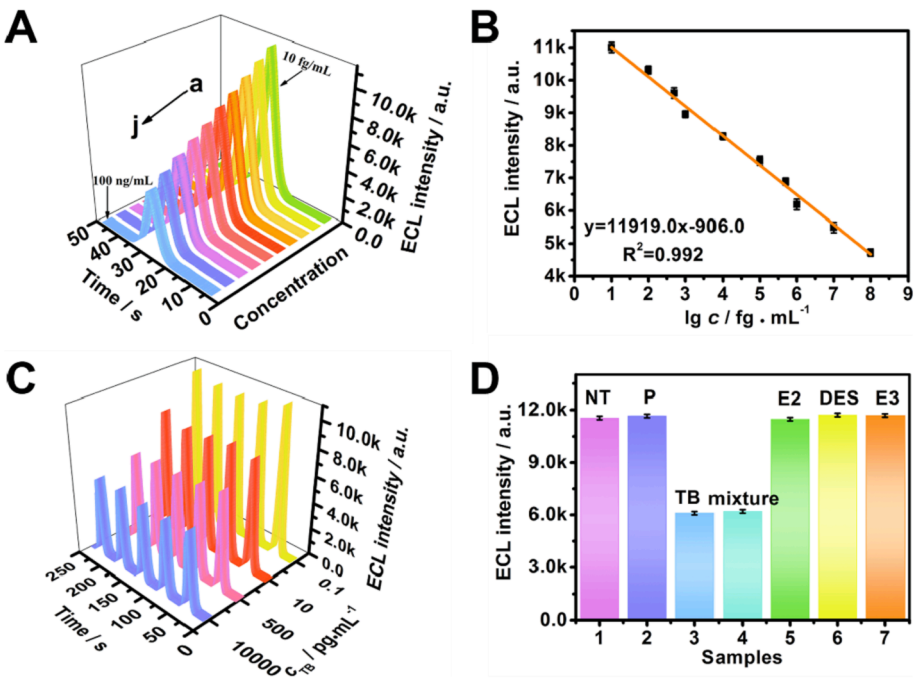

Fig. 4. (A) ECL intensity-time curves with a wide concentration range (curves a → j: 10 fg/mL, 100 fg/mL, 500 fg/mL, 1 pg/mL, 10 pg/mL, 100 pg/mL, 500 pg/mL, 1 ng/mL, 10 ng/mL and 100 ng/mL) and (B) the corresponding linear equation of the constructed ECL sensor for TB detection.(C) Stability of the constructed ECL sensor with different concentrations of TB under the same working times. (D) Selectivity tests under various interferences (10 ng/mL) of progesterone (P), estradiol (E2), estriol (E3), diethylstilbestrol (DES), nortestosterone (NT) and 1 ng/mL of TB. Error bars = SD, (n = 3). All experiments were carried out under optimal conditions.

In addition to ECL signals of the constructed sensor, stability and other performances are also the important criterions to measure its practicality. Firstly, we showed several detection signals of different concentrations of TB in a period of time (Fig. 4C), the ECL signals can always keep an equilibrium state, which verified the good stability of the constructed sensor. Secondly, very small differences between seven electrodes were observed in Fig. S9, verified the good reproducibility with the relative standard deviation (RSD) of 3.1%. Thirdly, the selectivity was tested in interferents (10 ng/mL) and mixture (1 ng/mL TB + 10 ng/mL interferents), the ECL signals were high about 11,500 a.u. and different from that in bare TB and mixture, which verified the outstanding selectivity of the constructed sensor (Fig. 4D). Finally, the feasibility of constructed ECL sensor for the analysis of real samples was inspected. The real water samples from three rivers were measured 3 times to obtain the initial concentrations. Then the accuracy and precision of the sensor were investigated by standard addition method for the initial sample. After 5 times testing, the recovery rates and RSD were calculated as 96.7–103% and 1.1–4.2% respectively, which confirmed the high accuracy and precision of the constructed ECL sensor. The relevant results were presented in Table S3. To summarize, the constructed ECL sensor has good stability, reproducibility, selectivity and practicability, and can well meet the needs of trace detection of environmental estrogen in the real environment.

4. Conclusion

In summary, we demonstrated a rare Eu(II)-MOF based on the reductant of glycine and the protectant of oleylamine, featuring high instantaneous anodic electroluminescence efficiency for trace detection of environmental estrogens. Remarkably, the ECL mechanism of the constructed sensor depended on TPA was understood by CV, ECL and other test methods. The dual self-enhancement mechanisms with the antenna effect of ligand to Eu^{2+} and the catalysis of Fe_3O_4-Ag NRs for TPA improved ECL signal and efficiency, which made the constructed sensor possess low LOD of 4.42 fg/mL and wide detection range of 10 fg/mL ~ 100 ng/mL. Moreover, the NIR luminescence characteristics of Eu(II)-Phen endowed the constructed sensor with working competence in harsh environment, therefore the ECL sensor is more suitable for the real environmental monitoring. This work not only provides a strategy to design and simply synthesize Eu(II)-MOF to avoid oxidation of Eu^{2+} into Eu^{3+} but also provides a platform for trace detection of enironmental estrogens to contribute to human health.

Declaration of Competing Interest

The authors declare that they have no known competing financial interests or personal relationships that could have appeared to influence the work reported in this paper.

Acknowledgments

This work was supported by the Young Taishan Scholars Program of Shandong Province (tsqn201909124), the National Natural Science Foundation of China (21775054), the Project of “20 items of University” of Jinan (2019GXRC018), the Innovation Team Project of Colleges and Universities in Jinan (no. 2019GXRC027). All of authors express their sincere thanks.

Appendix A. Supplementary data

Chemicals and reagents, Characterization and measurement equipments, XPS survey spectrum of as-prepared Eu(II)-Phen, XRD patterns of as-synthesized and simulated Eu(II)-Phen, EDS spectrum of as-prepared Fe_3O_4-Ag NRs, SEM image and elemental mapping of Ag, Fe and O for Fe_3O_4-Ag NRs, XPS spectra of as-prepared Fe_3O_4-Ag NRs, CV curves and linear relations of modified electrodes, Optimization of experimental conditions, Electrochemical performance of the biosensor, Repeatability of the biosensor under the detection of seven different electrodes, Comparison of ECL efficiency of different luminophors, Comparison of sensitivity of different methods for trenbolone detection, Standard addition data of purposed ECL sensor for trenbolone detection. Supplementary data to this article can be found online at https://doi.org/10.1016/j.cej.2022.136912.

References

[1] X. Zhang, G. Tian, W. Yin, L. Wang, X. Zheng, L. Yan, J. Li, H. Su, C. Chen, Z. Gu, Y. Zhao, Controllable generation of nitric oxide by near-infrared-sensitized

upconversion nanoparticles for tumor therapy, Adv. Funct. Mater. 25 (20) (2015) 3049–3056.
[2] Y. Kawamura, Y. Wada, S. Yanagida, Near-infrared photoluminescence and electroluminescence of neodymium(III), erbium(III), and ytterbium(III) complexes, Jpn. J. Appl. Phys. 40 (Part 1, No. 1) (2001) 350–356.
[3] B.D. Stringer, L.M. Quan, P.J. Barnard, C.F. Hogan, Electrochemically sensitized luminescence from lanthanides in *d–f* heteronuclear arrays, ChemPhotoChem. 2 (2018) 27–33.
[4] H.B. Wei, Z.F. Zhao, C. Wei, G. Yu, Z.W. Liu, B. Zhang, J. Bian, Z.Q. Bian, C. H. Huang, Antiphotobleaching: A Type of structurally rigid chromophore ready for constructing highly luminescent and highly photostable europium complexes, Adv. Funct. Mater. 26 (2016) 2085–2096.
[5] J.C.G. Bünzli, C. Piguet, Taking advantage of luminescent lanthanide ions, Chem. Soc. Rev. 34 (2005) 1048–1077.
[6] S.V. Eliseeva, J.-C. Bünzli, Lanthanide luminescence for functional materials and bio-sciences, Chem. Soc. Rev. 39 (1) (2010) 189–227.
[7] M.N. Wu, Y.X. Zhuang, J.B. Liu, W.W. Chen, X.Y. Li, R.J. Xie, Ratiometric fluorescence detection of 2,6-pyridine dicarboxylic acid with a dual-emitting lanthanide metal-organic framework (MOF), Opt Mater. 106 (2020), 110006.
[8] L.u. Zhao, X. Kuang, C. Chen, X.u. Sun, Z. Wang, Q. Wei, Boosting electrocatalytic nitrogen fixation via energy-efficient anodic oxidation of sodium gluconate, Chem. Commun. 55 (68) (2019) 10170–10173.
[9] X. Song, L.u. Zhao, C. Luo, X. Ren, L. Yang, Q. Wei, Peptide-based biosensor with a luminescent copper-based metal-organic framework as an electrochemiluminescence emitter for trypsin assay, Anal. Chem. 93 (28) (2021) 9704–9710.
[10] L. Zhao, X.Z. Song, X. Ren, H. Wang, D.W. Fan, D. Wu, Q. Wei, Ultrasensitive near-infrared electrochemiluminescence biosensor derived from Eu-MOF with antenna effect and high efficiency catalysis of specific CoS_2 hollow triple shelled nanoboxes for procalcitonin, Biosens Bioelectron. 191 (2021), 113409.
[11] L.u. Zhao, X. Song, X. Ren, D. Fan, Q. Wei, D. Wu, Rare self-luminous mixed-valence Eu-MOF with a self-enhanced characteristic as a near-infrared fluorescent ECL probe for nondestructive immunodetection, Anal. Chem. 93 (24) (2021) 8613–8621.
[12] L. Zhao, M. Wang, X.Z. Song, X.J. Liu, H.X. Ju, H.Q. Ai, Q. Wei, D. Wu, Annihilation luminescent Eu-MOF as a near-infrared electrochemiluminescence probe for trace detection of trenbolone, Chem Eng J. 434 (2022), 134691.
[13] D. Dutczak, T. Jüstel, C. Ronda, A. Meijerink, Eu^{2+} Luminescence in strontium aluminates, Phys. Chem. Chem. Phys. 17 (23) (2015) 15236–15249.
[14] J. Zhou, Z.G. Xia, M. Bettinelli, Q.L. Liu, Photoluminescence tuning via energy transfer in the Eu-doped Ba_2(Gd, $Tb_1 2Si4_{O1}3$ solid-solution phosphors, RSC Adv. 6 (2016) 2046–2054.
[15] N.B. Mikheev, L.N. Auerman, I.A. Rumer, A.N. Kamenskaya, M.Z. Kazakevich, The anomalous stabilisation of the oxidation state 2+ of lanthanides and actinides, Russ. Chem. Rev. 61 (10) (1992) 990–998.
[16] J.Y. Li, L.D. Wang, Z.F. Zhao, B.X. Sun, G. Zhan, H.Y. Liu, Z.Q. Bian, Z.W. Liu, Highly efficient and air-stable Eu(II)-containing azacryptates ready for organic light-emitting diodes, Nat Commun. 11 (2020) 5218–5225.
[17] T.N. Poe, M.J. Beltrán-Leiva, C. Celis-Barros, W.L. Nelson, J.M. Sperling, R. E. Baumbach, H. Ramanantoanina, M. Speldrich, T.E. Albrecht-Schönzart, Understanding the stabilization and tunability of divalent europium 2.2.2B cryptates, Inorg. Chem. 60 (11) (2021) 7815–7826.
[18] X. Ai, E.W. Evans, S. Dong, A.J. Gillett, H. Guo, Y. Chen, T.J.H. Hele, R.H. Friend, F. Li, Efficient radical-based light-emitting diodes with doublet emission, Nature 563 (7732) (2018) 536–540.
[19] A. Obolda, X. Ai, M. Zhang, F. Li, Up to 100% formation ratio of doublet exciton in deep-red organic light-emitting diodes based on neutral pi-radical, ACS Appl. Mater. Interfaces 8 (2016) 35472–35478.
[20] P. Dorenbos, Anomalous luminescence of Eu^{2+} and Yb^{2+} in inorganic compounds, J. Phys.: Condens. Matter 15 (2003) 2645–2665.
[21] Y. Wang, G. Zhao, H. Chi, S. Yang, Q. Niu, D. Wu, W. Cao, T. Li, H. Ma, Q. Wei, Self-luminescent lanthanide metal-organic frameworks as signal probes in electrochemiluminescence immunoassay, J. Am. Chem. Soc. 143 (1) (2021) 504–512.
[22] X. Song, T. Wu, C. Luo, L.u. Zhao, X. Ren, Y. Zhang, Q. Wei, Peptide-based electrochemiluminescence biosensors using silver nanoclusters as signal probes and Pd-Cu_2O hybrid nanoconcaves as coreactant promoters for immunoassays, Anal. Chem. 93 (38) (2021) 13045–13053.
[23] X.Z. Song, X.J. Li, D. Wei, R. Feng, T. Yan, Y.G. Wang, X. Ren, B. Du, H.M. Ma, Q. Wei, CuS as Co-reaction accelerator in PTCA-$K_2S_2O_8$ system for enhancing electrochemiluminescence behavior of PTCA and its application in detection of amyloid-β protein, Biosens Bioelectron. 126 (2019) 222–229.
[24] J.L. Wang, Z.Y. Bai, Fe-based catalysts for heterogeneous catalytic ozonation of emerging contaminants in water and wastewater, Chem. Eng. J. 312 (2017) 79–98.
[25] J.C. Li, Y. Hu, J. Yang, P. Wei, W.J. Sun, M.W. Shen, G.X. Zhang, X.Y. Shi, Hyaluronic acid-modified Fe_3O_4@Au core/shell nanostars for multimodal imaging and photothermal therapy of tumors, Biomaterials 38 (2015) 10–21.
[26] J. Li, Y. He, W. Sun, Y.u. Luo, H. Cai, Y. Pan, M. Shen, J. Xia, X. Shi, Hyaluronic acid-modified hydrothermally synthesized iron oxide nanoparticles for targeted tumor MR imaging, Biomaterials 35 (11) (2014) 3666–3677.
[27] Y. Liu, Y.Y. Zhang, Q.W. Kou, Y. Chen, D.L. Han, D.D. Wang, Z.Y. Lu, L. Chen, J. H. Yang, S. Xing, Eco-friendly seeded Fe_3O_4-Ag nanocrystals: a new type of highly efficient and low cost catalyst for methylene blue reduction, RSC Adv. 8 (2018) 2209–2218.
[28] F.L. Zhang, L. Kong, A.H. Zhao, W. Ge, Z.H. Yan, L. Li, M. De Felici, W. Shen, Inflammatory cytokines as key players of apoptosis induced by environmental estrogens in the ovary, Environ Res. 198 (2021), 111225.
[29] G.T. Ankley, D. Feifarek, B. Blackwell, J.E. Cavallin, K.M. Jensen, M.D. Kahl, S. Poole, E. Randolph, T. Saari, D.L. Villeneuve, Re-evaluating the significance of estrone as an environmental estrogen, Environ. Sci. Technol. 51 (8) (2017) 4705–4713.
[30] D. Wood, S. Shaw, T. Cawte, E. Shanen, B.V. Heyst, An overview of photocatalyst immobilization methods for air pollution remediation, Chem Eng J. 391 (2020), 123490.
[31] S.Z. Zhang, Z.H. Jiao, X. Zhao, M.Z. Sun, X.Z. Feng, Environmental exposure to 17β-trenbolone during adolescence inhibits social interaction in male mice, Environ Pollut. 289 (2021), 117710.
[32] G.D. Jones, P.V. Benchetler, K.W. Tate, E.P. Kolodziej, Mass balance approaches to characterizing the leaching potential of trenbolone acetate metabolites in agro-ecosystems, Environ. Sci. Technol. 48 (7) (2014) 3715–3723.
[33] F. Ma, D. Liu, 17β-trenbolone, an anabolic-androgenic steroid as well as an environmental hormone, Contributes to Neurodegeneration, Toxicol Appl Pharm. 282 (1) (2015) 68–76.
[34] F. Fang, Y.-Q. Li, G.-W. Huang, H.-M. Xiao, Q.-P. Feng, N. Hu, S.-Y. Fu, Electrical anisotropy and multidimensional pressure sensor of aligned Fe_3O_4@Silver nanowire/polyaniline composite films under an extremely low magnetic field, RSC Adv. 7 (8) (2017) 4260–4268.
[35] D. Kim, Y.-H. Jin, K.-W. Jeon, S. Kim, S.-J. Kim, O.H. Han, D.-K. Seo, J.-C. Park, Blue-silica by Eu^{2+}-activator occupied in interstitial sites, RSC Adv. 5 (91) (2015) 74790–74801.
[36] X. Liu, Y. Hu, B. Wang, Z. Su, Synthesis and fluorescent properties of europium-polymer complexes containing 1,10-phenanthroline, Synthetic Met. 159 (15-16) (2009) 1557–1562.
[37] D. Wang, C. Zheng, L. Fan, J. Zheng, X. Wei, Preparation and fluorescent properties of europium (III) complexes with β-diketone ligand and 2,2-dipyridine or 1,10-phenanthroline, Synthetic Met. 162 (23) (2012) 2063–2068.
[38] X.Z. Song, L. Zhao, C.N. Luo, X. Ren, X.Y. Wang, L. Yang, Q. Wei, Bioactivity-protective electrochemiluminescence sensor using CeO_2/Co_4N heterostructures as highly effective coreaction accelerators for ultrasensitive immunodetection, Sensor Actuat B-Chem. 355 (2022), 131158.
[39] Y. Kitagawa, Marina. Kumagai, P. P. F. Da Rosa, K. Fushimia, Y. Hasegawa, First Demonstration of the π–f Orbital Interaction Depending on the Coordination Geometry in Eu(III) Luminophores, Dalton Trans. 49 (2020) 3098-3101.
[40] Y.C. Wang, J.Y. Ding, Y.Y. Li, Y.H. Wang, Synthesis, structure and photoluminescent properties of a novel colortunable $Si_{1.92}Al_{0.08}O_{1.08}N_{1.92}$: Eu^{2+}, Tb^{3+}, Sm^{2+} phosphor for ultraviolet white light-emitting diodes, RSC Adv. 5 (2015) 88477–88484.
[41] Y. Wang, M.G. Brik, P. Dorenbos, Y. Huang, Y.e. Tao, H. Liang, Enhanced green emission of Eu^{2+} by energy transfer from the $^5D_3$ level of Tb^{3+} in $NaCaPO_4$, J. Phys. Chem. C. 118 (13) (2014) 7002–7009.
[42] Z. Guo, J. Xu, J. Zhang, Y. Hu, Y. Pan, P. Miao, Facile strategy for electrochemical analysis of hydrogen peroxide based on multifunctional Fe_3O_4@Ag nanocomposites, ACS Appl. Bio Mater. 1 (2) (2018) 367–373.
[43] H. Wang, J. Shen, G.X. Cao, Z. Gai, K.L. Hong, P.R. Debata, P. Banerjee, S.Q. Zhou, Multifunctional PEG encapsulated Fe_3O_4@Silver hybrid nanoparticles: antibacterial activity, cell imaging and combined photothermo/chemo-therapy, J. Mater. Chem. B. 1 (2013) 6225–6234.
[44] Q. Du, L. Tan, B.o. Li, T. Liu, J. Ren, Z. Huang, F. Tang, X. Meng, One-pot gradient solvothermal synthesis of the Ag/Au-Fe_3O_4 composite nanoparticles and their applications, RSC Adv. 4 (99) (2014) 56057–56062.
[45] Q. Xia, S. Fu, G. Ren, F. Chai, J. Jiang, F. Qu, Fabrication of magnetic bimetallic Fe_3O_4@Au-Pd hybrid nanoparticles with recyclable and efficient catalytic properties, RSC Adv. 6 (60) (2016) 55248–55256.
[46] D.a. Zhu, Y. Zhang, S. Bao, N. Wang, S. Yu, R. Luo, J. Ma, H. Ju, J. Lei, Dual intrareticular oxidation of mixed-ligand metal-organic frameworks for stepwise electrochemiluminescence, J. Am. Chem. Soc. 143 (8) (2021) 3049–3053.
[47] N. Zhang, X.T. Wang, Z.P. Xiong, L.Y. Huang, Y. Jin, A.J. Wang, P.X. Yuan, Y.B. He, J.J. Feng, Hydrogen bond organic frameworks as a novel electrochemiluminescence luminophore: simple synthesis and ultrasensitive biosensing, Anal. Chem. 93 (2021) 17110–17118.
[48] Y.J. Huang, Y.R. Pan, G. Du, Y.X. Cao, Extended structures of two coordination polymers based on 1,10-phenanthroline derivatives: preparation, structural characterization and properties, J. Chem. Sci. 128 (2016) 459–465.